

Solar energetic electron events with a spectral bump break

Wenyan Li¹, Linghua Wang^{1,*}, Wen Wang², Yang Su³, Säm Krucker^{4,5}, and Glenn M. Mason⁶

¹ School of Earth and Space Sciences, Peking University, Beijing, 100871, China

² College of Meteorology and Oceanography, National University of Defense Technology, Changsha, 410015, China

³ Key Laboratory of Dark Matter and Space Astronomy, Purple Mountain Observatory, Chinese Academy of Sciences, Nanjing 210023, China

⁴ Institute of 4D Technologies, University of Applied Sciences Northwestern Switzerland, 5210 Windisch, Switzerland

⁵ Space Sciences Laboratory, University of California, Berkeley, CA 94720, USA

⁶ Applied Physics Laboratory, Johns Hopkins University, Laurel, MD 20723 USA

Received 11 December 2024 / Accepted 24 April 2025

ABSTRACT

Aims. We present ten solar energetic electron (SEE) events measured by Wind/3DP at ~1 to 200 keV with a bump break in the electron peak flux versus energy spectrum. We examined their acceleration sources and/or processes at the Sun.

Methods. We assumed that these bump SEE events consist of two electron populations: a primary population (described by the pan-spectrum (PS) function), and a bump population (described by the Gaussian function), which dominate at low and high energies, respectively. We constructed two formulae to fit the SEE energy spectrum by multiplying a PS function with a natural exponential form of the Gaussian function (i.e., the MUL formula) and by adding a PS function with a Gaussian function (i.e., the ADD formula).

Results. The fitting results suggest that the MUL fitting can reflect the physical nature in the formation of these bump events. For the primary electron population, the MUL fitting obtains an upward-bending double power-law spectrum for event 10 with a spectral index of 3.58 (1.74) at energies below (above) ~4.6 keV, and a single power-law spectrum for the other nine events with a median spectral index of $2.52^{+0.29}_{-0.25}$. For the bump electron population, the fitted center energy has a median value of $59.1^{+18.1}_{-3.2}$ keV. For the events associated with soft X-ray flares (west limb coronal mass ejections), the flare class (angular width of the coronal mass ejection) is positively correlated with the estimated electron number of the power-law population N_{pl} and of the bump population N_{bp} (the number ratio N_{bp}/N_{pl} at 10–400 keV).

Conclusions. These results indicate that for these bump SEE events, the power-law electron population can be produced by some flare-related processes that occur high in the corona, while the bump population can be accelerated by some processes related to coronal mass ejections that act on the power-law population. The bump-like spectrum might also be the intermediate spectrum during the evolution from single power-law to downward-bending double power-law.

Key words. Sun: coronal mass ejections (CMEs) – Sun: flares – Sun: particle emission – Sun: radio radiation

1. Introduction

Solar energetic electron (SEE) events belong to the most common solar particle acceleration phenomena in the interplanetary medium (IPM) (Wang et al. 2016). Based on a statistical timing study of 1191 SEE events observed by the Wind 3D Plasma and Energetic Particle (3DP) instrument, Wang et al. (2012) reported that all SEE events have an ~76% association with ACE ³He-rich (³He/⁴He ≥ 0.01) ions, an ~36% association with GOES soft X-ray (SXR) flares, and an ~62% association with SOHO coronal mass ejections (CMEs) that take off from the solar west limb, as well as an ~99% association with type III radio bursts, but only an ~8% association with type II bursts. In addition, the >15 keV SEE events exhibit a ~45% association with hard X-ray (HXR) flares, while the estimated number ratio of the SEEs and HXR-producing electrons (HPEs) is only ~0.2%–2% at energies above 50 keV (e.g., Lin 1985; Krucker et al. 2007; Wang et al. 2021). Many case studies also found that some ³He-rich SEE events are accompanied by narrow CMEs or coronal jets that originate from flaring active regions in the western hemisphere (e.g., Pick et al.

2006; Nitta et al. 2008; Bučik 2020; Wang et al. 2023a). Therefore, SEEs likely arise from multiple origins and/or acceleration mechanisms.

At 1 au, the observed temporal flux profiles of SEE events typically exhibit a fast-rise, fast-decay peak with a clear velocity dispersion (i.e., faster electrons arrive earlier at the spacecraft than slower electrons), which is indicative of an essentially scatter-free propagation from the Sun to 1 au for most electrons in these events (Lin 1985; Wang et al. 2011). Thus, the SEE peak flux versus energy spectrum observed in situ carries crucial information on the origin and/or acceleration of SEEs at the Sun. Using the self-consistent pan-spectrum (PS) fitting method (Liu et al. 2020), Wang et al. (2023b) reported that 23 of the 458 SEE events detected with a clear velocity dispersion at energies from ≤4.2 keV to ≥108 keV showed a single power-law (SPL) energy spectrum with a median spectral index of $2.8^{+0.5}_{-0.2}$. Furthermore, 304 events exhibited a double power-law energy spectrum that bent downward at a break energy E_B with a median low-energy spectral index of $2.1^{+0.3}_{-0.3}$ and a high-energy spectral index of $3.7^{+0.6}_{-0.5}$. These are referred to as DDPL events. The DDPL events are further divided into two types: DDPL $_{E_B \geq 20 \text{ keV}}$ (74%) and DDPL $_{E_B < 20 \text{ keV}}$ (26%), since

* Corresponding author: wanglh@pku.edu.cn, wanglh@gmail.com

their E_B distribution shows a major peak at 61 keV and secondary peak at 5.6 keV. These peaks are separated by a dip at around 20 keV. For the DDPL $_{E_B \geq 20 \text{ keV}}$ type, the low-energy spectral index is positively correlated with the high-energy spectral index, but these spectral indexes do not appear to be correlated with E_B . For the DDPL $_{E_B < 20 \text{ keV}}$ type, however, the low-energy spectral index shows no correlation with the high-energy spectral index, and these spectral indexes are positively correlated with E_B . Furthermore, $\sim 7\%$ of the 458 events have an upward-bending double-power-law (UDPL) spectrum with a median spectral index of $3.0^{+0.3}_{-0.3}$ at energies below E_B near 5.1 keV and a spectral index of $2.2^{+0.2}_{-0.3}$ at energies above E_B . For the UDPL type, the low-energy spectral index is also positively correlated with the high-energy spectral index, while these spectral indexes appear to be negatively correlated with E_B . These different relations among the spectral parameters suggest that the formation of SEE events involves complex sources and/or acceleration processes at the Sun.

Some SEE events clearly exhibit an unusual bump-like spectral break at tens of keV that was not reported by previous observational studies. This bump spectrum can shed new light on the SEE origin and acceleration. In this paper, we identify ten good SEE events observed by Wind/3DP with a clear spectral bump at no fewer than three energy channels (Section 2.1). After constructing the spectral fitting functions, we examine the spectral features of these bump events (Section 2.2 and 2.3), as well as their relation with other solar phenomena, including flares, west limb CMEs, radio bursts, and the $^3\text{He}/^4\text{He}$ ratio (Section 2.4) and their comparison with general power-law SEE events (Section 2.5).

2. Observations

Since the launch of the Wind spacecraft in November 1994, the onboard 3DP instrument has been nominally operating to measure the full three-dimensional electron distributions in the solar wind at energies from thermal plasma to ~ 400 keV with an angular resolution of 22.5° (Lin et al. 1995). In Wind/3DP, silicon semiconductor telescopes (SSTs) detect the ~ 25 – 400 keV electrons with an energy channel resolution of $\Delta E/E \approx 0.3$ and a time resolution of 12 sec, while electrostatic analyzers (EESA-L and EESA-H) observe the ~ 3 eV– 30 keV electrons with an energy channel resolution of $\Delta E/E \approx 0.2$ and a time resolution of 96 sec (Wang et al. 2012).

2.1. Event selection

We found that 43 of the 458 SEE events observed by Wind/3DP with a velocity dispersion over a wide energy range (Wang et al. 2023b) have a bump-like spectral break that is characterized by a peak around tens of keV in the derivative of $\Delta(\ln J)/\Delta(\ln E)$ (see, e.g., Figure 1b), where J is the electron background-subtracted peak differential flux in the energy channel centered at E . In order to unambiguously investigate the characteristics of this spectral break, we further identified ten good events observed at energies of ~ 1 – 200 keV with an electron peak flux higher than twice the pre-event background flux, a clear velocity dispersion in the peak fluxes, and a bump-like spectral break that clearly occurred at no fewer than three energy channels (Table A.1) out of the 43 bump events. The bump-like spectral break cannot be well described by the PS formula, which is designed with a smooth derivative of $d(\ln J)/d(\ln E)$ (Liu et al. 2020, also see the dashed lines in Figure 1b).

Figure 1 plots the representative events 5 (10) that were observed with a clear velocity dispersion of the peak fluxes

at 430 eV–310 keV (630 eV–180 keV) on October 20, 2002 (February 20, 2014). The observed antisunward-traveling electrons are beamed along the interplanetary magnetic field (IMF) (see Figure 1f) with a pitch-angle width at all energies that is similar to the general SEE events (Wang et al. 2011). These features indicate that most of the SEEs undergo nearly scatter-free propagation from the Sun to 1 au, and thus, the peak flux energy spectrum that is observed in situ can reflect the physical nature of the electron acceleration at the Sun (Wang et al. 2011, 2016, 2023b). For event 5 (10), the background-subtracted peak flux versus energy spectrum exhibits a bump-like break with fluxes that are significantly higher than the PS fitting at energies of ~ 40 – 200 keV (~ 30 – 100 keV), as well as a power-law shape that is described well by the PS fitting at other energies.

2.2. Spectrum fitting

For simplicity, we assumed that these bump SEE events consist of two electron populations: a primary population and bump population, which appear to dominate at low and high energies, respectively. We used the PS function to characterize the spectral features of the primary electron population and a Gaussian function of $\ln E$ to quantify the center energy and energy range of the bump electron population. We constructed two new fitting formulae by multiplying the PS function with a natural exponential form of Gaussian function (referred to as the MUL formula, as demonstrated by Figures 1c and g) and by adding a PS function with a Gaussian function (referred to as the ADD formula, as demonstrated in Figures 1d and h) as follows:

$$\text{MUL formula: } J(E) = A_1 \times E^{-\beta_1} \left[1 + \left(\frac{E}{E_{\text{pl}}} \right)^\alpha \right]^{\frac{\beta_1 - \beta_2}{\alpha}} \times \exp \left[A_2 \times e^{-\frac{(\ln E - \ln E_{\text{bp}})^2}{2\sigma^2}} \right]; \quad (1.1)$$

$$\text{ADD formula: } J(E) = A_1 \times E^{-\beta_1} \left[1 + \left(\frac{E}{E_{\text{pl}}} \right)^\alpha \right]^{\frac{\beta_1 - \beta_2}{\alpha}} + A_2 \times e^{-\frac{(\ln E - \ln E_{\text{bp}})^2}{2\sigma^2}}, \quad (1.2)$$

where E is the electron energy in eV, and J is the differential flux in $\text{cm}^{-2} \text{ s}^{-1} \text{ sr}^{-1} \text{ eV}^{-1}$. The MUL formula indicates that the bump electron population results from a secondary acceleration process acting on the primary electron population, while the ADD formula suggests that the bump population is caused by an independent acceleration process.

For the primary (PS) population, β_1 (β_2) is the power-law spectral index at energies below (above) the power-law break centered at E_{pl} , and α (>0) describes the sharpness and width of the break. With these parameters, the PS spectrum can be self-consistently determined to be a power-law, Ellison-Ramaty, Kappa, or logarithmic-parabola distribution (Liu et al. 2020; Wang et al. 2023b). For the bump population, E_{bp} is the center energy. The energy interval with respect to the full width at half maximum is defined as $I_{\text{bp}} = E_{\text{bp}} \times [e^{-\sqrt{2\ln 2}\sigma}, e^{\sqrt{2\ln 2}\sigma}]$, that is, the peak-trough distance in the derivative of $d(\ln J)/d(\ln E)$ (Figure 1b), and its energy width is $W_{\text{bp}} = E_{\text{bp}} \times [e^{\sqrt{2\ln 2}\sigma} - e^{-\sqrt{2\ln 2}\sigma}]$.

For the selected ten bump events, we fit the observed J versus E spectrum to both the MUL and ADD formulae after considering the uncertainties in the energy and flux and using the nonlinear least-square method (Liu et al. 2020). According to the fitted parameters, the primary population agrees with the power-law

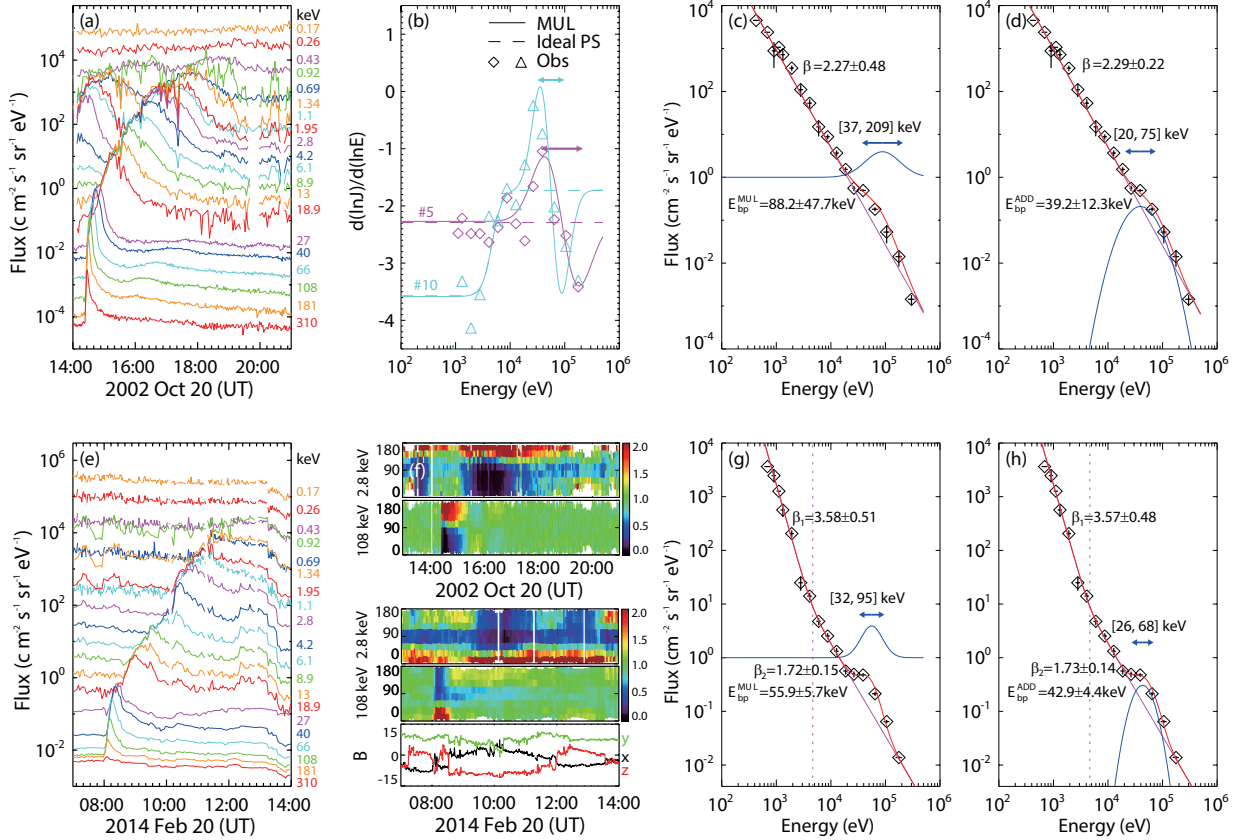


Fig. 1. Overview of the bump SEE events on October 20, 2002 (event 5) and February 20, 2014 (event 10). Panels (a) and (e): Flux time profiles of outward-traveling electrons observed by EESA-L (0.17–1.1 keV, 3 min average), EESA-H (0.92–18.9 keV, 3 min average), and SST (27–310 keV, 90 sec average) for events 5 and 10. Panel (b): Derivative of $\Delta(\ln J)/\Delta(\ln E)$ for event 5 (purple diamonds) and 10 (cyan triangles), where J is the electron background-subtracted peak differential flux. The solid (dashed) line shows the derivative from the MUL (PS) fitting results. Panels (c) and (g): ADD fitting to the observed electron peak flux energy spectrum for events 5 and 10. Panels (d) and (h): MUL fitting. The red lines in panels (c–d) and (g–h) indicate the total fitting results, and the blue (purple) lines represent the Gaussian (PS) portion in fitting. In panels (b–d) and (g–h), the double-ended arrows show the FWHM of the Gaussian portion in the MUL or ADD fittings. Panel (f): Electron pitch-angle distributions normalized at each time bin and 2.8 (108) keV for events 5 and 10, and three components of the IMF vector for event 10. The beamed distributions exhibit higher values (red) in the beaming direction and lower values (indigo) in the other directions, while isotropic distributions exhibit normalized values around one (green) in all directions. The typical peak interval for the ten bump SEE events is about 12 (3) minutes at low energies (high energies).

spectral shape (i.e., also called as the power-law population) for all these events. Moreover, the power-law spectral shape can be classified as SPL, UDPL and DDPL when $\beta_1 \approx, >$ and $< \beta_2$. For event 5 on October 20, 2002 (Figures 1c–d), the power-law population was fitted to an SPL energy spectrum with a spectral index of $\beta^{\text{MUL}} = 2.27 \pm 0.48$ ($\beta^{\text{ADD}} = 2.29 \pm 0.22$), and the bump population was characterized by a center energy of $E_{\text{bp}}^{\text{MUL}} = 88 \text{ keV}$ ($E_{\text{bp}}^{\text{ADD}} = 39 \text{ keV}$) and an energy interval of $J_{\text{bp}}^{\text{MUL}} = [37, 209] \text{ keV}$ ($J_{\text{bp}}^{\text{ADD}} = [20, 75] \text{ keV}$) for the MUL (ADD) fitting. For event 10 on February 20, 2014 (Figures 1g–h), the power-law electron population was described by a UDPL energy spectrum with a low-energy spectral index of $\beta_1^{\text{MUL}} = 3.58 \pm 0.51$ ($\beta_1^{\text{ADD}} = 3.57 \pm 0.48$) at energies below $E_{\text{pl}}^{\text{MUL}} = 4.6 \pm 1.5 \text{ keV}$ ($E_{\text{pl}}^{\text{ADD}} = 4.7 \pm 1.6 \text{ keV}$) and a high-energy spectral index of $\beta_2^{\text{MUL}} = 1.74 \pm 0.15$ ($\beta_2^{\text{ADD}} = 1.73 \pm 0.14$) at energies above E_{B} , while the bump population was characterized by a center energy of $E_{\text{bp}}^{\text{MUL}} = 56 \text{ keV}$ ($E_{\text{bp}}^{\text{ADD}} = 43 \text{ keV}$) and an energy range of $J_{\text{bp}}^{\text{MUL}} = [32, 95] \text{ keV}$ ($J_{\text{bp}}^{\text{ADD}} = [26, 68] \text{ keV}$).

Table A.1 lists the fitted spectral characteristics, and Figure 2 plots the distributions of these characteristics, with their correlation coefficients (CCs) presented (also see Figures 6a–c). For

the power-law electron population, the fitted spectral parameters are mostly consistent between the MUL and ADD fittings (Table A.1 and Figure 2). For nine events with the exception of event 10 (Figures 2a and e), they are fitted well by an SPL spectrum with a spectral index β^{MUL} (β^{ADD}) that ranges from ~ 1.9 to ~ 3.7 (~ 3.6), with a median value of $2.52^{+0.29}_{-0.25}$ ($2.54^{+0.23}_{-0.11}$).

For the bump electron population, the estimated center energy E_{bp} does not appear to be correlated between the MUL and ADD fittings (Table A.1 and Figure 2f). $E_{\text{bp}}^{\text{MUL}}$ ($E_{\text{bp}}^{\text{ADD}}$) varies from $\sim 44 \text{ keV}$ to $\sim 171 \text{ keV}$ (from $\sim 21 \text{ keV}$ to $\sim 43 \text{ keV}$) with a median value of $59.1^{+18.1}_{-3.2} \text{ keV}$ ($25.1^{+3.2}_{-3.5} \text{ keV}$), while $E_{\text{bp}}^{\text{MUL}}$ is about 1.3–10.6 times as high as $E_{\text{bp}}^{\text{ADD}}$ (Figures 2b and f). However, the fitted energy width W_{bp} , as well as the $W_{\text{bp}}/E_{\text{bp}}$ ratio, is strongly correlated for the MUL and ADD fittings. $W_{\text{bp}}^{\text{MUL}}$ ($W_{\text{bp}}^{\text{ADD}}$) ranges from $\sim 63 \text{ keV}$ to $\sim 587 \text{ keV}$ (from $\sim 27 \text{ keV}$ to $\sim 55 \text{ keV}$) with a median value of $172^{+53}_{-45} \text{ keV}$ (37^{+3}_{-2} keV), while $W_{\text{bp}}^{\text{MUL}}$ is about 1.5–17.1 times as high as $W_{\text{bp}}^{\text{ADD}}$ (Figures 2c and g). The $W_{\text{bp}}^{\text{MUL}}/E_{\text{bp}}^{\text{MUL}}$ ($W_{\text{bp}}^{\text{ADD}}/E_{\text{bp}}^{\text{ADD}}$) ratio extends from ~ 1.1 to ~ 3.4 (from ~ 1.0 to ~ 2.1), with a median value of $2.9^{+0.1}_{-0.8}$ ($1.4^{+0.3}_{-0.1}$) (Figures 2d and h).

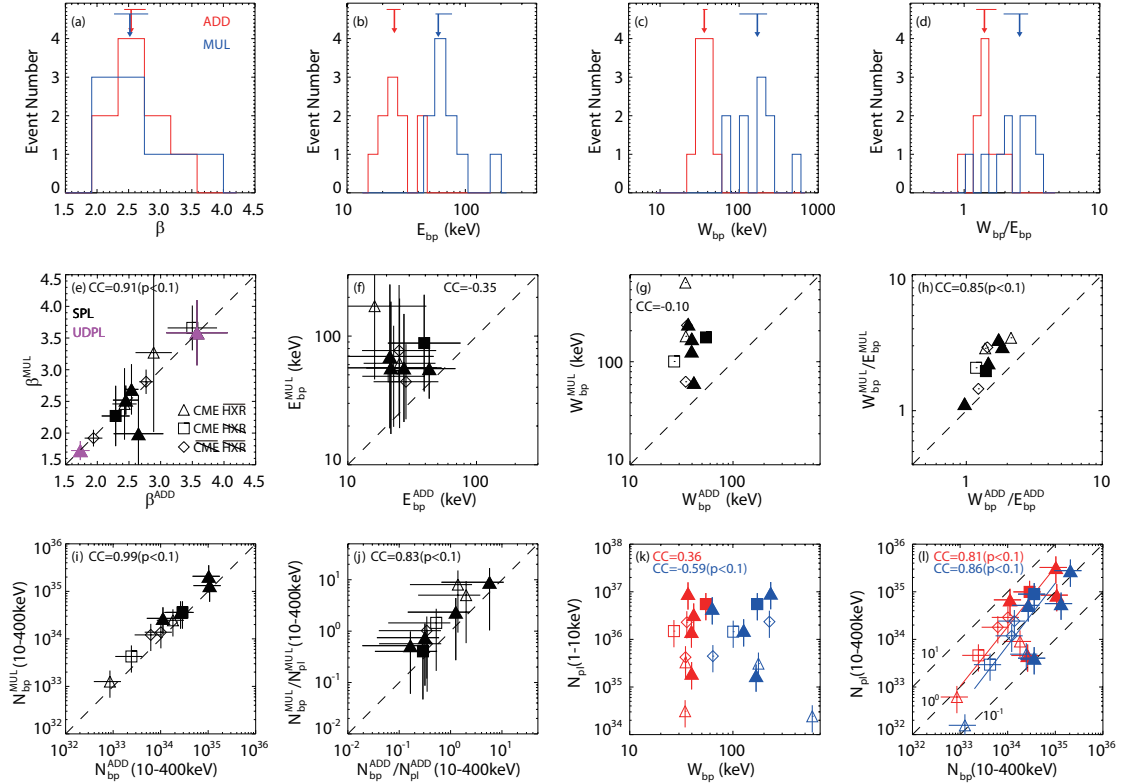


Fig. 2. Histograms and scatter diagrams for the spectral parameters of the selected ten bump SEE events. Panels (a–d): Histograms of β , E_{bp} , W_{bp} , and W_{bp}/E_{bp} estimated from the ADD (red) and MUL (blue) fittings. The arrows with horizontal bars indicate the median values with their first and third quartiles. Panel (a) only plots the nine events (1–9) with a fitted SPL spectral shape for the primary population. Panels (e–h): Scatter plots of β , E_{bp} , W_{bp} , and W_{bp}/E_{bp} between the ADD and MUL fittings. Panels (i–j): Same format for N_{bp} and N_{bp}/N_{pl} at 10–400 keV. In panels (e–j), the dashed lines indicate the 1:1 ratio. Panel (k): W_{bp} vs. N_{pl} at 1–10 keV. Panel (l): N_{bp} vs. N_{pl} at 10–400 keV. The dashed lines denote the ratios of 10^1 , 10^0 , and 10^{-1} . The solid red (blue) line denotes the estimated linear regression of $N_{pl}^{ADD} \propto 3.34N_{bp}^{ADD}$ ($N_{pl}^{MUL} \propto 1.54N_{bp}^{MUL}$) for the ten bump events. In panels (e–l), the triangles indicate the bump SEE events associated with west limb CMEs and with HXR flares or no available HXR measurements, the squares represent the SEE events with west limb CMEs and no HXR flares (when measurements are available), and the diamonds show the events without west limb CMEs and HXR flares (when measurements are available), or events without available CME and HXR measurements. The solid (open) symbols indicate events associated with (without) type II radio bursts. We used the logarithm of the electron number to calculate the CCs regarding the electron number.

Moreover, we obtained the background-subtracted fluence versus energy spectrum by integrating the electron flux over the duration at one-third of the background-subtracted peak flux for each event. After fitting these fluence spectra to the MUL and ADD formulae, we estimated the electron number of the power-law and bump populations by integrating the corresponding function over a given energy range and the spatial extent of a 45° cone in the IPM (Wang et al. 2012, 2021). At 10–400 keV (Table A.1), the integrated electron number N_{pl}^{MUL} (N_{pl}^{ADD}) ranges from 1.6×10^{32} to 2.8×10^{35} (from 6.2×10^{32} to 3.2×10^{35}) for the fitted power-law population, while N_{bp}^{MUL} (N_{bp}^{ADD}) varies from 1.3×10^{33} to 2.1×10^{35} (from 8.6×10^{32} to 1.1×10^{35}) for the fitted bump population (Figure 2i). The number ratio of $N_{bp}^{MUL}/N_{pl}^{MUL}$ ($N_{bp}^{ADD}/N_{pl}^{ADD}$) ranges from 0.3 to 8.9 (from 0.2 to 5.7) with a median value of $1.02^{+4.00}_{-0.55}$ ($0.35^{+1.04}_{-0.03}$) (Figure 2j). These electron number estimates (N_{bp} , N_{pl} or N_{bp}/N_{pl}) are all clearly positively correlated for the MUL and ADD fittings, and at 10–400 keV, there is a linear regression of $N_{pl}^{MUL} \propto 1.54N_{bp}^{MUL}$ ($N_{pl}^{ADD} \propto 3.34N_{bp}^{ADD}$) that we show in Figure 2l.

For the ten events at 10–400 keV (Figure 2l), the estimated electron number N_{bp}^{MUL} (N_{bp}^{ADD}) is positively correlated with N_{pl}^{MUL} (N_{pl}^{ADD}). This positive correlation also appears to be present for all 43 bump events (not shown), although the spec-

tral bump break of most of them is weaker than in the selected ten events we studied. These results suggest that the production of the bump electron population is likely related to the power-law population, that is, they favor the physical implication of the MUL fitting function.

2.3. Height estimate of the solar source

The low-energy spectral shape of SEEs observed in situ carries the information on the height of their solar source. As suggested by (Wang et al. 2006), SEEs can experience energy loss due to the Coulomb collision and the ambipolar electrostatic potential during their propagation from the Sun to the IPM,

$$\frac{dE}{dr} = \left(\frac{dE}{dr}\right)_{COL} + \left(\frac{dE}{dr}\right)_{AEP} = -0.182 \frac{n(r)}{E} - \frac{994}{r^2}, \quad (2)$$

where r is the heliocentric distance in solar radius R_s . The electron density $n(r)$ in cm^{-3} is described by the plasma density model (Wang et al. 2021; Mann et al. 1999) as

$$n(r) = \begin{cases} 2.0 \times 10^9 e^{13.83(\frac{1}{r}-1)} & 1.02 < r \leq 3 \\ 3.3 \times 10^5 r^{-2} + 4.1 \times 10^6 r^{-4} + 8.0 \times 10^7 r^{-6} & 3 \leq r < 215. \end{cases} \quad (3)$$

Figure 3 shows the simulated peak flux versus energy spectra at 1 au resulting from an SPL source spectrum at the Sun. Due to

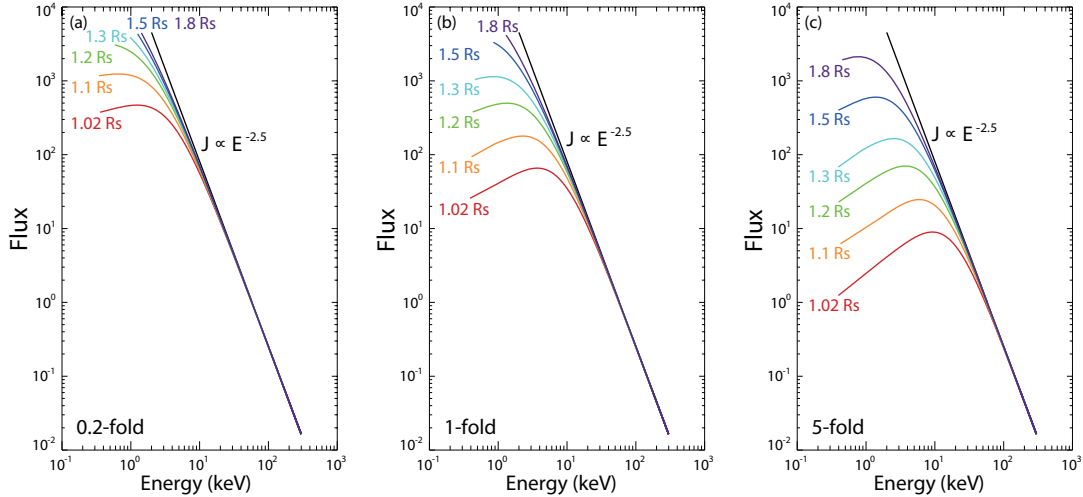


Fig. 3. Simulated electron spectra at 1 au derived from an SPL spectrum injected at different r , after considering the electron energy loss due to Coulomb collisions with the 0.2-fold, 1-fold and 5-fold electron density models and due to the ambipolar electrostatic potential between the Sun and IPM. The injected spectral index of 2.5 is the median index value of the power-law electron populations in the selected bump SEE events. We applied the 0.2-fold and 5-fold density models to estimate the uncertainties of the source height that are caused by varying the magnitude of density model.

the energy loss during the propagation (Equation 2), the spectral shape at 1 au would bend downward at energies below a cut-off energy. This cutoff energy increases with decreasing source height or increasing magnitude of the density model. The ten SEE events we studied all show a power-law spectrum that is observed in situ at low energies extending to <1 keV, suggesting that their solar source likely lies high in the corona, for instance, $\geq 1.5 R_S$ from the solar center. This is consistent with previous studies (Lin et al. 1996; Wang et al. 2006, 2021).

2.4. Association with other solar phenomena

As suggested by Wang et al. (2012), the electron release time at the Sun, T_{rel} , was estimated with uncertainties of ± 10 minutes by subtracting the travel time along a nominal 1.2 AU path length from the onset time observed in the highest energy channel of the event at 1 au. For each event, we identified a possibly associated SXR flare observed by GOES when the SXR impulsive phase overlapped with T_{rel} within ± 10 minutes (Wang et al. 2012), an associated HXR flare observed by RHESSI when the HXR peak time agreed with T_{rel} within ± 20 minutes (Wang et al. 2021), and an associated CME observed by SOHO/LASCO when the CME took off from the solar west limb with an estimated height within $10 R_S$ above the photosphere at T_{rel} (Wang et al. 2012). In addition, the associated SXR and HXR flares were required to be located close to the footpoint of connecting magnetic field lines that were estimated by potential-field sources surface (PFSS) model, when the flare location was available.

Eight of the ten bump events (Table A.2; 80%) were associated with an SXR flare, including seven impulsive flares and one gradual flare with a class ranging from C1.0 to M5.1. The median flare class intensity was $C6.0^{+26.5}_{-3.4}$, and the median duration was $21^{+21}_{-10.5}$ min. Of the SEE spectral parameters from the MUL and ADD fittings, the associated flare class intensity shows no obvious correlation with the power-law spectral index β and bump center energy E_{bp} , but it is positively correlated with the estimated electron number of the power-law population (N_{pl}) and of the bump population (N_{bp}) (Figure 5).

Five out of the eight SEE events with available RHESSI observations ($\sim 63\%$) were accompanied by HXR flares (Table

A.2). Three events lack reliable HXR measurements during the flare peak phase (due to the effects of a night orbit, the South Atlantic Anomaly, and/or penetrating particles); the other two events on November 12, 2013 (event 9) and February 20, 2014 (event 10) exhibit good peak HXR observations, each with two HXR peaks separated by <5 minutes (marked P1 and P2 in Figure 4). Figure 4 plots the photon flux energy spectra, as well as the X-ray contours reconstructed with the CLEAN algorithm (Hurford et al. 2002), averaged over the peak interval of these HXR flares associated with the two bump events. The background-subtracted photon peak flux spectrum fits a thermal component and a broken power-law with a spectral index of 1.5 at energies below the break. Assuming a single power-law energy spectrum of HPEs, we used the relativistic thick-target bremsstrahlung model to estimate the HPE power-law spectral index β^{HPE} and the total number N^{HPE} during the peak interval.

For the November 12, 2013 SEE event (top panels of Figure 4), the HXR P1 (P2) peak at $\sim 21:31$ UT ($\sim 21:33$ UT) shows one nonthermal source located roughly along with the thermal source, likely due to inadequate spatial resolution; the estimated β^{HPE} is 6.7 ± 0.2 (4.0 ± 1.1), which is higher than the spectral index of SEE power-law population. At 15–400 keV, N^{HPE} is about 1.7×10^{36} (1.3×10^{36}) and is 65 times (50 times) higher than the number of SEE power-law populations N_{pl} . For the February 20, 2014 SEE event (bottom panels of Figure 4), the P1 (P2) HXR peak at $\sim 07:36$ UT ($\sim 07:41$ UT) exhibits two footpoint nonthermal sources; the estimated β^{HPE} is 4.5 ± 0.1 (5.5 ± 0.1), which is higher than the spectral index of the SEE power-law population at both low energies and high energies. At 10–400 keV, N^{HPE} is about 1.7×10^{37} (1.5×10^{37}) and it is 170 times (150 times) higher than the total number of SEE power-law population N_{pl} . All these HXR peaks/bursts were accompanied by EUV jets measured by SDO/AIA.

Eight of the nine bump SEE events with available SOHO/LASCO observations ($\sim 89\%$) were associated with a CME, including two halo CMEs with a speed of $V_{\text{CME}} \sim 960$ km/s and six west limb CMEs with a $V_{\text{CME}} \sim 300$ –1200 km/s and an angular width of $W_{\text{CME}} \sim 15^\circ$ – 125° . The median CME speed was 941^{+49}_{-298} km/s and the median CME width (without the two halo CMEs) was 61^{+46}_{-34} , which is similar to those asso-

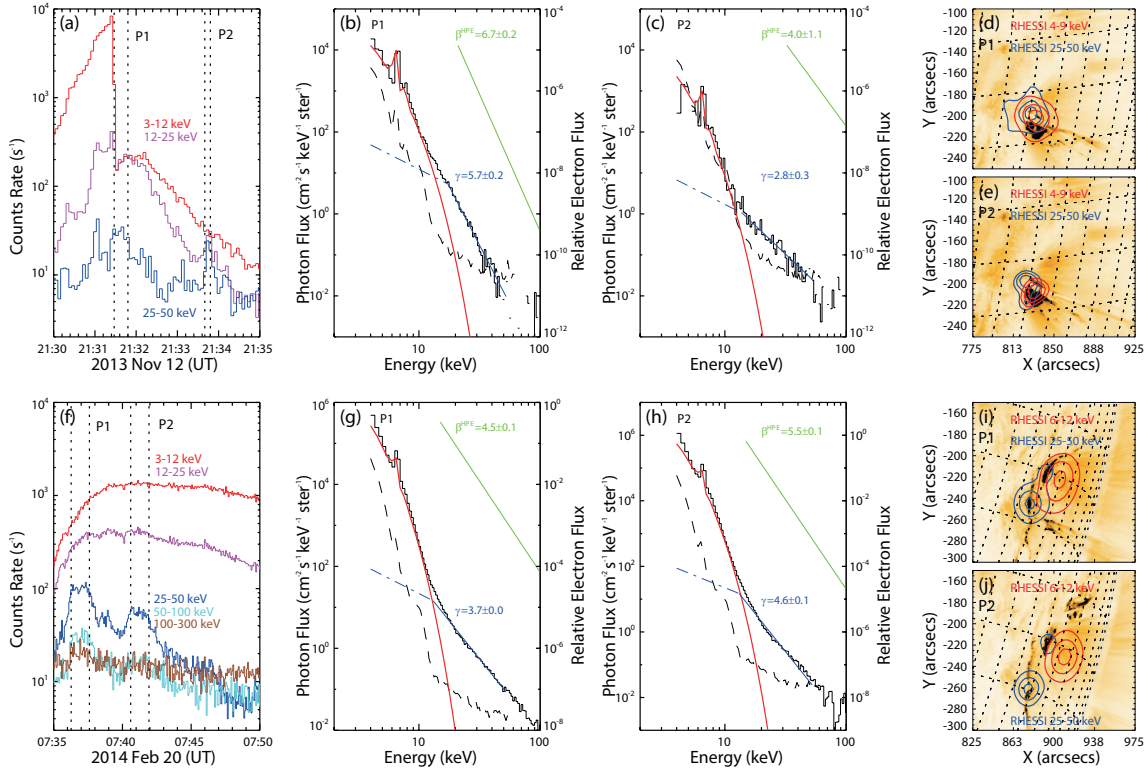


Fig. 4. RHESSI HXR flares associated with the bump SEE events on November 12, 2013 (event 9; top panels) and February 20, 2014 (event 10; bottom panels). Panels (a) and (f): X-ray light curves. The vertical dashed lines mark the two emission peak intervals (P1 and P2) of the HXR flare. Panels (b) and (g): Spectrum of the photon peak flux vs. energy (solid black line) measured during P1. The solid blue (red) line represents an SPL fit (the thermal fit) to observations at energies above 20 keV (below 15 keV), and the dashed blue line shows an SPL with a fixed index of 1.5 at energies below 20 keV as an approximation of nonthermal emissions at these energies. The green line represents the estimated SPL spectrum of HPEs (multiplied by an arbitrary factor for display). Panels (c) and (h): Same format for P2. Panels (d) and (i): RHESSI CLEAN X-ray intensity contours at levels of 40%, 60%, and 80% measured during P1, plotted on the SDO/AIA image at 171 Å. Panels (e) and (j): Same format for P2.

ciated with the $DDPL_{E_B \geq 20 \text{ keV}}$ SEE events at energies from ≤ 4.2 keV to ≥ 108 keV (Wang et al. 2024). Figure 5 shows the correlations between the CME parameters and the SEE spectral parameters for the eight events (see also Figures 6d–e). For the MUL and ADD fittings, the estimated electron number ratio, N_{bp}/N_{pl} , of the bump and power-law (primary) populations is correlated with W_{CME} , while no spectral parameters are correlated with V_{CME} or with the CME kinetic energy K_{CME} (Figures 6d–e). However, $N_{bp}^{ADD}/N_{pl}^{ADD}$ is strongly correlated with $N_{bp}^{MUL}/N_{pl}^{MUL}$, which likely leads to the association between $N_{bp}^{ADD}/N_{pl}^{ADD}$ and W_{CME} .

Type II radio bursts are a good indicator of shock electron acceleration. Two of the ten bump events (Table A.2) were accompanied by a type II radio burst that was observed at metric wavelengths (30 MHz–300 MHz) by ground-based stations and at decametric-hectometric wavelengths (DH, 300 kHz–30 MHz) by Wind/WAVES, and three were only associated with a metric type II burst. The heliocentric burst height can be roughly estimated from the plasma frequency with the electron density distribution model (Equation (3)). Figure 7 shows that these type II radio bursts can be generated at ~ 1.1 – $1.7 R_S$ for metric emissions and at ~ 2 – $13 R_S$ for DH emissions (also see Table A.2). However, the selected SEE events in this study probably do not support a significant contribution from the shock acceleration, different from gradual SEE events. In addition, all ten bump SEE events were associated with type III radio bursts. This is consistent with the previous statistical study of all the SEE events by Wang et al. (2012).

Figure 2 shows that the bump SEE events with (solid symbols) and without (open symbols) type II radio bursts behave similarly in the values of β (the spectral index of the power-law electron population), E_{bp} (the center energy of the bump population), and W_{bp} (the bump energy width). However, the bump SEE events with type II bursts mostly show a larger N_{pl} (the electron number of power-law population) and N_{bp} (the electron number of bump population), but the N_{bp}/N_{pl} ratio is similar, compared to the bump events without type II bursts (Figures 2 and 5). In addition, the bump events with type II radio bursts appear to be associated with a stronger SXR flare, but with a similar CME property, for example, V_{CME} , W_{CME} , and K_{CME} (not shown), compared to the bump events without type II bursts (Table A.2 and Figure 5). Figure 5 also shows that the bump SEE events with and without type II radio bursts behave differently in the relations between the spectral index β and SXR class and between N_{bp}/N_{pl} and V_{CME} . For bump events with (without) type II bursts, β exhibits no clear correlation (a negative correlation) with the SXR class; the N_{bp}/N_{pl} ratio shows a negative correlation (no obvious correlation) with V_{CME} .

Eight out of the ten bump SEE events have available ion measurements by ACE/ULEIS (Table A.2). As defined by Wang et al. (2012), we used a time interval to calculate the associated ${}^3\text{He}/{}^4\text{He}$ ratio at ~ 0.5 – 2 MeV nucleon $^{-1}$: $[T_{rel}+5h, T_{rel}+9h]$, or $[T_{rel}+5h, T_{rel}^{**}+5h]$ (when $T_{rel}^{**}+5h$ occurred earlier than $T_{rel}+9h$), where T_{rel}^{**} is the estimated release time of the subsequent event in the entire SEE event list of Wind/3DP (e.g., Wang et al. 2012, 2023b). Six of the eight bump events

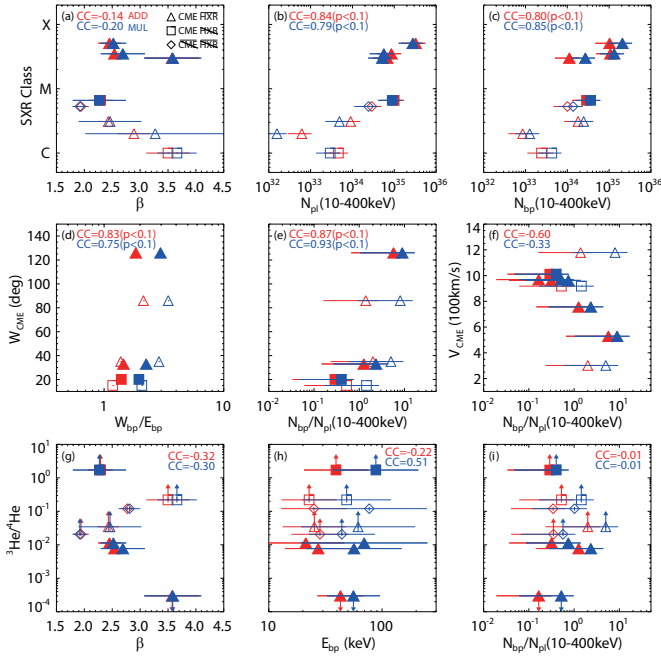


Fig. 5. Scatter diagrams of the parameters between the ten bump SEE events and the associated solar phenomena, including SXR flares (top), west limb CMEs (middle), and $^3\text{He}^4\text{He}$ (bottom). Panels (a–c): SXR class vs. β , $N_{\text{bp}}/N_{\text{pl}}$ at 10–400 keV and N_{bp} at 10–400 keV. Panels (d–e): CME width vs. $W_{\text{bp}}/E_{\text{bp}}$, $N_{\text{bp}}/N_{\text{pl}}$ at 10–400 keV. Panel (f): CME speed vs. $N_{\text{bp}}/N_{\text{pl}}$ at 10–400 keV. Panels (g–h): $^3\text{He}^4\text{He}$ ratio vs. β and E_{bp} . Panel (i): $^3\text{He}^4\text{He}$ ratio vs. $N_{\text{bp}}/N_{\text{pl}}$ at 10–400 keV. The upward (downward) arrows indicate the underestimated (overestimated) $^3\text{He}^4\text{He}$ ratio. In all panels, blue (red) shows the SEE parameters from the MUL (ADD) fitting. The symbols represent the same as in Figure 2. We used the logarithm of the electron number and of $^3\text{He}^4\text{He}$ ratio to calculate the corresponding CCs.

(75%) were accompanied by ^3He -rich ion emissions with a $^3\text{He}^4\text{He}$ ratio ≥ 0.01 , similar to the statistical study of SEE events (Wang et al. 2012). As shown by Figures 5g–i and 6d–e, the $^3\text{He}^4\text{He}$ ratio shows no obvious correlation with all the SEE parameters estimated from the MUL and ADD fittings or with the CME parameters and SXR flare class. These results disagree with the results of Hart et al. (2024), who reported that ^3He -rich solar energetic particle events associated with fast (>450 km/s) and wide ($>45^\circ$) CMEs tend to have a higher $^3\text{He}^4\text{He}$ ratio than those with slow and wide CMEs. However, the measured $^3\text{He}^4\text{He}$ ratio in four bump SEE events (1, 4, 5 and 9) is underestimated since the ^4He measurements are dominated by the previous large solar energetic particle event; the $^3\text{He}^4\text{He}$ ratio in event 10 gives an upper-limit estimate.

For the bump SEE events without type II radio bursts (open symbols in Figure 5), however, the $^3\text{He}^4\text{He}$ ratio is positively correlated with β^{MUL} and β^{ADD} , which is consistent with the previous study by Wang et al. (2021). For bump SEE events with type II radio bursts (solid symbols), the $^3\text{He}^4\text{He}$ ratio perhaps shows a negative correlation with β^{MUL} and β^{ADD} , while it tends to have a positive correlation with $E_{\text{bp}}^{\text{MUL}}$ and no clear correlation with $E_{\text{bp}}^{\text{ADD}}$. Future studies would require a large number of events to further understand the possible role of shocks (indicated by type II bursts) in the formation of SEEs and ^3He -rich ions.

2.5. Comparison with general power-law SEE events

Based on the statistical study by Wang et al. (2023b), about 78% of SEE events detected at energies from ≤ 4.2 keV to ≥ 108 keV exhibit a power-law spectral shape, including the SPL ($\sim 5\%$), UDPL ($\sim 7\%$), DDPL $_{E_{\text{B}} < 20 \text{ keV}}$ ($\sim 16\%$), and DDPL $_{E_{\text{B}} \geq 20 \text{ keV}}$ ($\sim 50\%$) types. Table A.3 compares the spectral parameters of ten bump SEE events from the MUL fitting with those of general SEE events with a power-law spectral shape. For the bump SEE events, the fitted primary (bump) electron population dominates at low (high) energies.

For nine bump SEE events (except event 10), the primary electron population shows a SPL shape with a median spectral index of $2.5^{+0.3}_{-0.3}$, which is slightly harder than the spectrum of SPL SEE type ($2.8^{+0.5}_{-0.2}$) and low-energy spectrum of UDPL type ($3.0^{+0.3}_{-0.3}$), but somewhat softer than the low-energy spectrum of DDPL $_{E_{\text{B}} < 20 \text{ keV}}$ type ($2.0^{+0.2}_{-0.2}$) and DDPL $_{E_{\text{B}} \geq 20 \text{ keV}}$ type ($2.1^{+0.3}_{-0.3}$). The bump electron population exhibits a median center energy of 61^{+16}_{-5} keV, which is similar to the spectral break energy of DDPL $_{E_{\text{B}} \geq 20 \text{ keV}}$ SEE type (61^{+23}_{-12} keV), but significantly higher than that of DDPL $_{E_{\text{B}} < 20 \text{ keV}}$ type ($5.6^{+2.3}_{-2.4}$ keV) and UDPL type ($5.1^{+4.2}_{-1.8}$ keV). On the other hand, the electron peak flux at 2.8 keV (dominated by the primary population) ranges between $[0.25, 12.6] \times 10^4 \text{ cm}^{-2} \text{ s}^{-1} \text{ sr}^{-1} \text{ keV}^{-1}$, while the electron peak flux at 108 keV (dominated by the bump population) varies from $0.6 \text{ cm}^{-2} \text{ s}^{-1} \text{ sr}^{-1} \text{ keV}^{-1}$ to $128 \text{ cm}^{-2} \text{ s}^{-1} \text{ sr}^{-1} \text{ keV}^{-1}$. This is similar to the DDPL $_{E_{\text{B}} < 20 \text{ keV}}$ and DDPL $_{E_{\text{B}} \geq 20 \text{ keV}}$ types (see Table A.3).

Based on the solar release timing, these nine bump events have a 79% association with SXR flares with a median class of C5.3 $^{+20.8}_{-2.5}$, a 57% association with HXR flares, and an 88% association with west limb CMEs (Table A.3). These associations are similar to those of UDPL, DDPL $_{E_{\text{B}} < 20 \text{ keV}}$, and DDPL $_{E_{\text{B}} \geq 20 \text{ keV}}$ SEE types, but they are probably higher than those of SPL type (Table A.3; Wang et al. 2024). The nine bump events also show an 11% association with interplanetary type II radio bursts, which is similar to the SPL and DDPL types, but lower than the UDPL type.

For bump SEE event 10, the primary electron population exhibits a UDPL shape with a spectral index of 3.58 ± 0.51 (1.74 ± 0.15) at energies below (above) a break energy of 4.6 ± 1.5 keV, consistent with the spectral parameters of UDPL SEE type (Table A.3). Its bump electron population shows a center energy of 56 ± 6 keV, which is similar to the break energy of DDPL $_{E_{\text{B}} \geq 20 \text{ keV}}$ type, but significantly higher than that of DDPL $_{E_{\text{B}} < 20 \text{ keV}}$ and UDPL types. The electron peak flux at 2.8 keV (dominated by the primary population) is $2.5 \times 10^4 \text{ cm}^{-2} \text{ s}^{-1} \text{ sr}^{-1} \text{ keV}^{-1}$ (also see Figure 1), which is similar to the four types of power-law SEE events. The electron peak flux at 108 keV (dominated by the bump population) is $64.6 \text{ cm}^{-2} \text{ s}^{-1} \text{ sr}^{-1} \text{ keV}^{-1}$, which is similar to the DDPL $_{E_{\text{B}} < 20 \text{ keV}}$ and DDPL $_{E_{\text{B}} \geq 20 \text{ keV}}$ SEE types, but (probably) higher than the SPL (UDPL) type. In addition, the bump SEE event 10 has an M3.0 SXR flare, an HXR flare, a west limb CME, and a type II radio burst.

3. Summary and discussion

We have comprehensively investigated ten bump SEE events observed by Wind/3DP at ~ 1 –200 keV from 1995 through 2019 in order to understand their source/acceleration at the Sun. For the SEE spectral fitting, we construct the MUL (ADD) formula, which is the multiplication (sum) of a PS function with a natural exponential form of Gaussian

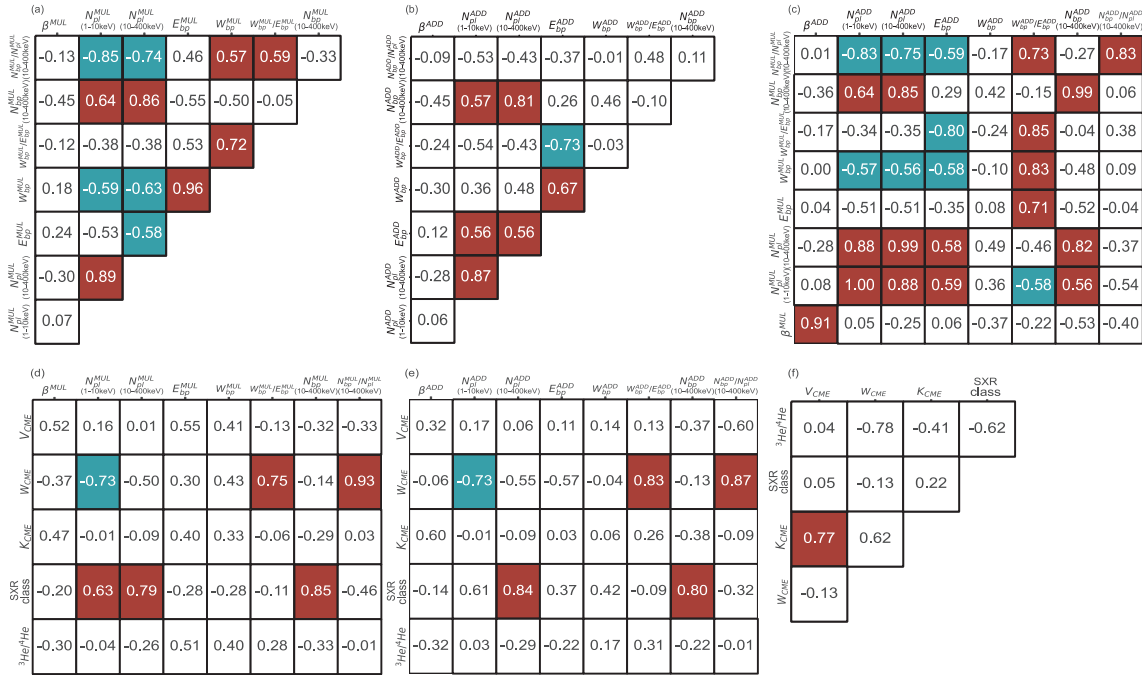


Fig. 6. Correlograms of the parameters between the ten bump SEE events and the associated solar phenomena including SXR flares, west limb CMEs, and ${}^3\text{He}/{}^4\text{He}$. Panel (a): Autocorrelation matrix between the SEE parameters estimated from the ADD fitting. Panel (b): Same format for the MUL fitting. Panel (c): Correlation matrix of SEE parameters between the ADD and MUL fittings. Panel (d): Correlation matrix between the ADD SEE parameters and the parameters of the associated solar phenomena. Panel (e): Same format for the MUL fitting. Panel (f): Autocorrelation matrix between the parameters of the solar phenomena. The CCs are listed in the center of each cell. The cell is color-coded when the CC is statistically significant ($p < 0.1$). Red (blue) indicates a positive (negative) correlation. For a statistically insignificant CC ($p \geq 0.1$), its cell is shown in white. We used the logarithm of the electron number and of ${}^3\text{He}/{}^4\text{He}$ ratio to calculate the corresponding CCs.

function (a Gaussian function), using the PS function to describe the features of primary electron population and a Gaussian function to characterize the center energy and energy range of the bump electron population. The MUL formula indicates that the bump electron population is caused by a secondary acceleration process acting on the primary population, while the ADD formula suggests that the bump population arises from an independent acceleration process. All the ten events fit the MUL and ADD formulae well when the uncertainties in energy and flux are taken into account (Figure 1). For the ADD fitting, however, the estimated electron number $N_{\text{bp}}^{\text{ADD}}$ exhibits a positive correlation with $N_{\text{pl}}^{\text{ADD}}$ (Figures 2 and 5), although the ADD formula assumes two independent electron groups of the PS population and the bump population. Therefore, the production of the bump electron population is likely related to the primary population, and the MUL fitting results can reflect the physical nature in the formation for these selected bump SEE events.

For the primary electron population that dominates at low energies of these selected SEE events (Figure 1 and Table A.1), the MUL fitting obtained a UDPL spectral shape for event 10 and an SPL shape for the other nine events. For event 10, the fitted power-law spectral index is $\beta_1^{\text{MUL}} = 3.58 \pm 0.51$ at energies below 4.6 ± 1.5 keV and $\beta_2^{\text{MUL}} = 1.74 \pm 0.15$ at energies above. For the other nine events, the fitted SPL spectral index has a median value of $2.52^{+0.29}_{-0.25}$. Thus, the primary electron populations is also referred to as the power-law population. As suggested by previous studies (Wang et al. 2006, 2021), the interplanetary detection of a power-law spectrum extending to ~ 1 keV favors an acceleration source high in the corona (Figure 3), for example, $\geq 1.5 R_{\text{S}}$ from the solar center. For the bump electron population that appears significant at high energies of

these SEE events, the fitted center energy $E_{\text{bp}}^{\text{MUL}}$ (energy width $W_{\text{bp}}^{\text{MUL}}$) ranges from ~ 44 keV to ~ 171 keV (from ~ 63 keV to ~ 587 keV) with a median value of $59.1^{+18.1}_{-3.2}$ keV (172^{+53}_{-45} keV). The $W_{\text{bp}}^{\text{MUL}}/E_{\text{bp}}^{\text{MUL}}$ ratio varies from ~ 1.1 to ~ 3.4 with a median value of $2.9^{+0.1}_{-0.8}$ (Figure 2). On the other hand, the estimated electron number ratio $N_{\text{bp}}/N_{\text{pl}}$ at 10–400 keV ranges from 0.3 to 8.9, with a median value of $1.02^{+4.00}_{-0.55}$.

Among the ten bump SEE events (when remote-sensing measurements are available; Table A.2 and A.3), 80% are associated with GOES SXR flares with an intensity class ranging from C.1 to M5.1, and $\sim 63\%$ have RHESSI HXR flares; $\sim 90\%$ are accompanied by SOHO west limb CMEs with a median angular width of 61^{+46}_{-34} (excluding halo CMEs) and median speed of 941^{+49}_{-298} km/s, while $\sim 50\%$ ($\sim 20\%$) have metric (DH) type II radio bursts. The two events (9 and 10) with good measurements from RHESSI and SDO/AIA both have two HXR emission peaks and two EUV jets, while the estimated power-law spectrum of HPes is steeper/softer than that of the power-law SEE population (Figures 1 and 4).

For the bump events associated with SXR flares (Figures 5 and 6), the flare class shows a positive correlation with the estimated electron number of power-law population N_{pl} and of the bump population N_{bp} , while N_{bp} is proportional to N_{pl} . For the events associated with west limb CMEs, the CME angular width (excluding halo CMEs) exhibits a positive correlation with the electron number ratio of $N_{\text{bp}}/N_{\text{pl}}$ at 10–400 keV, as well as with the $W_{\text{bp}}/E_{\text{bp}}$ ratio, and it shows a negative correlation with N_{pl} . The SXR class is not correlated with the CME angular width. In addition, the bump SEE events without type II radio bursts have a negative correlation between β (the spectral index of the

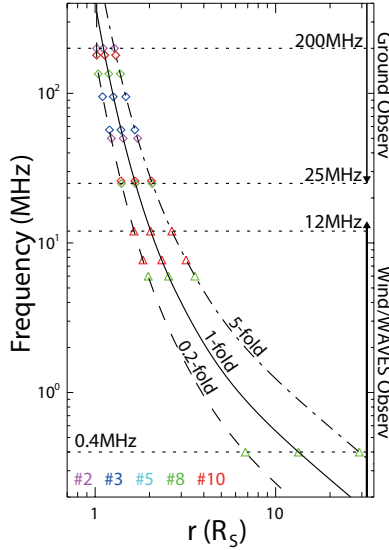


Fig. 7. Variation in the type II burst height r with plasma frequency estimated from the electron density model of Equation (3). The dashed, dotted, and dash-dotted curves represent the 0.2-fold, 1-fold, and 5-fold models, respectively. The colored symbols indicate the lower and upper bounds of the burst frequency range observed by ground-based stations and by Wind/WAVES for different bump SEE events.

power-law electron population) and SXR class, while bump events with type II radio bursts show a negative correlation between the $N_{\text{bp}}/N_{\text{pl}}$ ratio and CME speed. These results indicate that for the ten bump SEE events, the power-law electron population can be produced by some flare-related processes that occur high in the corona, and the bump population can be accelerated by some CME-related processes acting on the power-law population. Therefore, the bump-like spectrum might be the intermediate spectrum during the evolution from the SPL spectrum to DDPL $_{E_{\text{B}} \geq 20 \text{ keV}}$ spectrum, as a result of some CME-related processes acting on the SPL electron population.

The bump SEE events with and without type II radio bursts behave similarly in the values of β (the spectral index of power-law electron population), E_{bp} (the center energy of bump population), W_{bp} (the bump energy width), and $N_{\text{bp}}/N_{\text{pl}}$. Furthermore, the $N_{\text{bp}}/N_{\text{pl}}$ ratio tends to increase with decreasing CME speed for bump events with type II radio bursts. These results suggest that the above CME-related processes may not involve the shock acceleration.

Recently, Wang et al. (2023b) reported that about 78% of SEE events that were detected at energies from ≤ 4.2 keV to ≥ 108 keV exhibited a power-law spectral shape, including four spectral types: SPL ($\sim 5\%$), UDPL ($\sim 7\%$), DDPL $_{E_{\text{B}} < 20 \text{ keV}}$ ($\sim 16\%$), and DDPL $_{E_{\text{B}} \geq 20 \text{ keV}}$ ($\sim 50\%$). Based on the correlation among the spectral parameters and on the relation between the spectral parameters and solar phenomena, Wang et al. (2024) proposed that the SPL type can arise from the initial acceleration process that likely occurs high in the corona, and then provides seed populations for further acceleration processes to form the other spectral types. For instance, the DDPL $_{E_{\text{B}} \geq 20 \text{ keV}}$ (DDPL $_{E_{\text{B}} < 20 \text{ keV}}$) type could be further accelerated by some CME-related (flare-related) processes, while the UDPL type is probably further accelerated by CME-driven shocks (probably at higher altitudes).

For the selected bump SEE events except for event 10 (Table A.3), the fitted power-law electron population shows an SPL energy spectrum with a median spectral index of $2.52^{+0.29}_{-0.25}$, which

is slightly lower than the typical spectral index of the SPL type ($2.8^{+0.5}_{-0.2}$) and is higher than the low-energy spectral index ($2.1^{+0.3}_{-0.3}$) of the DDPL $_{E_{\text{B}} \geq 20 \text{ keV}}$ type. The fitted bump population exhibits a median center energy of $59.1^{+18.1}_{-3.2}$ keV, similar to the break of the DDPL $_{E_{\text{B}} \geq 20 \text{ keV}}$ type. At all energies, the electron peak fluxes at low energies appear to be similar to the fluxes of the DDPL $_{E_{\text{B}} \geq 20 \text{ keV}}$ type. At low energies (high energies), the electron peak fluxes do not appear to be lower than (higher than) those of the SPL type. Moreover, these bump SEE events behave similarly in the association with SXR flares, west limb CMEs and DH type II radio bursts as the SPL and DDPL $_{E_{\text{B}} \geq 20 \text{ keV}}$ types. Therefore, the bump-like spectrum might be the intermediate spectrum during the evolution from the SPL spectrum to the DDPL $_{E_{\text{B}} \geq 20 \text{ keV}}$ spectrum, as a result of some CME-related processes that act on the SPL electron population. The particle-in-cell plasma simulations by Riquelme et al. (2022) recently suggested that a spectral bump near 150–300 keV can be produced by the electron acceleration by temperature anisotropy instabilities at above-the-loop-top sources in solar flares. Future studies with a larger number of bump SEE events, as well as detailed simulations, will help us to further understand the formation and evolution of SEE events at the Sun.

Acknowledgements. This research at Peking University is supported in part by NSFC under contracts 42225404, 42127803 and 42150105, by National Key R&D Program of China No. 2021YFA0718600, and by ISSI-BJ and ISSI through the international teams Nos. 23-581 and 56. The research at JHU/APL is supported by NASA contract 80NSSC22K0374.

References

- Bučík, R. 2020, *Space Sci. Rev.*, **216**, 24
 Chen, B., Bastian, T. S., Shen, C., et al. 2015, *Science*, **350**, 1238
 Drake, J., Swisdak, M., Che, H., & Shay, M. 2006, *Nature*, **443**, 553
 Dulk, G. A., Leblanc, Y., Bastian, T., & Bougeret, J.-L. 2000, *J. Geophys. Res.*, **105**, 27343
 Haggerty, D. K., & Roelof, E. C. 2008, *ApJ*, **579**, 841
 Hart, S. T., Dayeh, M. A., Bučík, R., et al. 2024, *ApJ*, **974**, 220
 Holman, G. 1985, *D.*, **107**, 191
 Holman, G. D., & Pesses, M. 1983, *ApJ*, **267**, 837
 Hurford, G. J., Schmahl, E. J., Schwartz, R. A., et al. 2002, *Sol. Phys.*, **210**, 61
 Krucker, S., Kontar, E., Christe, S., & Lin, R. 2007, *ApJ*, **663**, L109
 Krucker, S., Oakley, P., & Lin, R. 2009, *ApJ*, **691**, 806
 Lin, R. 1985, *Sol. Phys.*, **100**, 537
 Lin, R., & Schwartz, R. 1987, *ApJ*, **312**, 462
 Lin, R., Anderson, K. A., Ashford, S., et al. 1995, *SSRv*, **71**, 125
 Lin, R. P., Larson, D., McFadden, J., et al. 1996, *Geophys. Res. Lett.*, **23**, 1211
 Lin, R. P., Dennis, B. R., Hurford, G. J., et al. 2002, *Sol. Phys.*, **210**, 3
 Liu, Z., Wang, L., Wimmer-Schweingruber, R. F., Krucker, S., & Mason, G. M. 2020, *J. Geophys. Res.*, **125**, e2020JA028702
 Mann, G., Jansen, F., MacDowall, R., Kaiser, M., & Stone, R. 1999, *A&A*, **348**, 614
 Mason, G. M., Ho, R. C., Allen, J., et al. 2021, *A&A*, **656**, L1
 Nitta, N. V., Mason, G. M., Wiedenbeck, M. E., et al. 2008, *ApJ*, **675**, L125
 Pick, M., Mason, G. M., Wang, Y.-M., Tan, C., & Wang, L. 2006, *ApJ*, **648**, 1247
 Press, W. H., Teukolsky, S. A., Vetterling, W. T., & Flannery, B. P. 2007, *Numerical recipes 3rd edition: The art of scientific computing* (Cambridge University Press)
 Riquelme, M., Osorio, A., Verscharen, D., & Sironi, L. 2022, *ApJ*, **924**, 52
 Wang, L., Lin, R. P., Krucker, S., & Gosling, J. T. 2006, *Geophys. Res. Lett.*, **33**, L03106
 Wang, L., Lin, R. P., & Krucker, S. 2011, *ApJ*, **727**, 121
 Wang, L., Lin, R., Krucker, S., & Mason, G. M. 2012, *ApJ*, **759**, 69
 Wang, L., Krucker, S., Mason, G. M., et al. 2016, *A&A*, **585**, A119
 Wang, W., Wang, L., Krucker, S., et al. 2021, *ApJ*, **913**, 89
 Wang, W., Battaglia, A. F., Krucker, S., et al. 2023a, *ApJ*, **950**, 118
 Wang, W., Wang, L., Krucker, S., Wimmer-Schweingruber, R. F., et al. 2023b, *ApJ*, **948**, 51
 Wang, W., Wang, L., Li, W., Krucker, S., Wimmer-Schweingruber, R. F., et al. 2024, *ApJ*, **969**, 164

Appendix A: Tables of ten bump SEE events

We list the fitted spectral parameters for the ten bump SEE events in Table A.1, the properties of other solar phenomena associated with these bump SEE events in Table A.2, and the comparison between the ten bump SEE events and general power-law SEE events in Table A.3.

Table A.1. The fitted parameters of 10 bump SEE events

#	Date	T_{rel}^a (UT)	β^{ADD}	E_{bp}^{ADD} (keV)	W_{bp}^{ADD} (keV)	I_{bp}^{ADD} (keV)	N_{pl}^{ADD} (1-10keV) (10^{36})	N_{pl}^{ADD} (10-400keV) (10^{34})	N_{bp}^{ADD} (10-400keV) (10^{34})	β^{MUL}	E_{bp}^{MUL} (keV)	W_{bp}^{MUL} (keV)	N_{bp}^{MUL} (keV)	N_{pl}^{MUL} (1-10keV) (10^{36})	N_{pl}^{MUL} (10-400keV) (10^{34})	N_{bp}^{MUL} (10-400keV) (10^{34})	$N_{pl}^{MUL}/N_{bp}^{MUL}$ (10-400keV)
1	1998-08-29	18:29	1.94 ± 0.14	28.3 ± 5.8	34.7	[15.9, 50.6]	$0.42^{+0.30}_{-0.23}$	$2.89^{+2.05}_{-1.57}$	$1.01^{+0.71}_{-0.55}$	$0.35^{+0.31}_{-0.31}$	44.2 ± 7.5	63.9	[22.6, 86.5]	$0.44^{+0.31}_{-0.24}$	$2.42^{+1.71}_{-1.32}$	$1.38^{+0.98}_{-0.75}$	$0.57^{+0.50}_{-0.50}$
2	2001-10-09	07:38	2.65 ± 0.39	21.6 ± 7.8	39.8	[9.5, 49.3]	$0.19^{+0.14}_{-0.11}$	$0.46^{+0.32}_{-0.25}$	$2.62^{+1.86}_{-1.42}$	$5.72^{+5.06}_{-5.06}$	56.7 ± 12.5	167.7	[17.4, 185.1]	$0.17^{+0.12}_{-0.09}$	$0.40^{+0.28}_{-0.22}$	$3.60^{+2.55}_{-1.95}$	$8.93^{+7.89}_{-7.89}$
3	2002-02-20	06:04	2.45 ± 0.20	21.2 ± 7.7	36.7	[9.7, 46.4]	$9.26^{+6.55}_{-5.02}$	$32.42^{+22.93}_{-17.59}$	$10.27^{+7.26}_{-5.57}$	$0.32^{+0.28}_{-0.28}$	69.5 ± 16.2	232.4	[19.2, 251.6]	$9.37^{+6.63}_{-5.09}$	$27.79^{+19.65}_{-15.08}$	$20.75^{+14.67}_{-11.26}$	$0.75^{+0.66}_{-0.66}$
4	2002-10-20	11:28	3.50 ± 0.39	22.7 ± 7.1	26.8	[13.0, 39.8]	$1.49^{+1.06}_{-0.81}$	$0.46^{+0.33}_{-0.25}$	$0.24^{+0.17}_{-0.13}$	$0.53^{+0.46}_{-0.46}$	48.7 ± 19.8	100.6	[19.7, 120.3]	$1.45^{+1.03}_{-0.79}$	$0.29^{+0.21}_{-0.16}$	$0.43^{+0.30}_{-0.23}$	$1.45^{+1.28}_{-1.28}$
5	2002-10-20	14:08	2.29 ± 0.22	39.2 ± 12.3	54.7	[20.5, 75.1]	$5.52^{+3.90}_{-2.99}$	$9.95^{+7.03}_{-5.40}$	$2.88^{+2.04}_{-1.56}$	$0.29^{+0.26}_{-0.26}$	88.2 ± 47.7	172.3	[37.1, 209.4]	$5.50^{+3.89}_{-2.99}$	$8.93^{+6.31}_{-4.84}$	$3.60^{+2.55}_{-1.95}$	$0.40^{+0.36}_{-0.36}$
6	2003-03-17	10:06	2.77 ± 0.11	25.0 ± 5.6	35.7	[12.9, 48.6]	$2.29^{+1.62}_{-1.24}$	$1.80^{+1.27}_{-0.98}$	$0.62^{+0.44}_{-0.34}$	$0.34^{+0.30}_{-0.30}$	77.2 ± 27.9	225.6	[23.9, 249.5]	$2.35^{+1.66}_{-1.28}$	$1.19^{+0.84}_{-0.64}$	$1.21^{+0.86}_{-0.66}$	$1.02^{+0.90}_{-0.90}$
7 ^b	2005-09-04	15:01	2.89 ± 0.29	16.1 ± 19.6	34.4	[6.4, 40.8]	$0.03^{+0.02}_{-0.02}$	$0.06^{+0.04}_{-0.03}$	$0.09^{+0.06}_{-0.05}$	$1.39^{+1.23}_{-1.23}$	170.9 ± 190.1	587.1	[46.1, 633.2]	$0.02^{+0.02}_{-0.01}$	$0.02^{+0.01}_{-0.01}$	$0.13^{+0.09}_{-0.07}$	$8.05^{+7.11}_{-7.11}$
8	2011-08-08	17:54	2.54 ± 0.11	27.3 ± 4.5	39.6	[13.9, 53.6]	$1.47^{+1.04}_{-0.80}$	$8.50^{+6.01}_{-4.61}$	$10.73^{+7.59}_{-5.82}$	$1.26^{+1.12}_{-1.12}$	56.5 ± 7.6	127.1	[21.5, 148.6]	$1.55^{+1.10}_{-0.84}$	$5.64^{+3.99}_{-3.06}$	$13.21^{+9.34}_{-7.17}$	$2.34^{+2.07}_{-2.07}$
9	2013-11-12	21:35	2.43 ± 0.19	25.2 ± 7.9	34.8	[13.3, 48.0]	$0.33^{+0.23}_{-0.18}$	$0.90^{+0.64}_{-0.49}$	$1.81^{+1.28}_{-0.98}$	$2.01^{+1.77}_{-1.77}$	61.5 ± 30.7	176.7	[19.3, 196.0]	$0.31^{+0.22}_{-0.17}$	$0.49^{+0.35}_{-0.27}$	$2.46^{+1.74}_{-1.33}$	$5.02^{+4.43}_{-4.43}$
10 ^c	2014-02-20	07:45	3.57 ± 0.48	42.9 ± 4.4	41.7	[26.9, 68.6]	$3.33^{+2.36}_{-1.81}$	$6.77^{+4.79}_{-3.67}$	$1.12^{+0.79}_{-0.61}$	$0.17^{+0.15}_{-0.15}$	55.9 ± 5.7	63.1	[32.6, 95.7]	$4.51^{+3.19}_{-2.48}$	$5.18^{+3.66}_{-2.81}$	$2.70^{+1.91}_{-1.47}$	$0.52^{+0.46}_{-0.46}$

Notes.

- (^a) Subtracted from the onset time in the event's highest energy channel detected in situ by the travel time along a nominal 1.2 AU path length.
(^b) Event 7 shows large uncertainties of β^{MUL} , caused by the very limited number of energy channels that are dominated by power-law population.
(^c) For event 10, the primary or PS population is fitted to a UDPL with the spectral index β_1 (β_2) at energies below (above) a break energy E_{pl} in both the MUL and ADD fittings.

Table A.2. Other solar phenomena associated with 10 bump SEE events

#	Date	SOHO West-Limb CME ^c				AIA Jet ^e		GOES SXR Flare ^f		RHESXI HXR Flare ^g		Type II ^h		³ He/ ⁴ He (%)	
		T _{rel} ^b (UT)	P.A. (deg)	Width (deg)	V (km/s)	K (erg)	T (UT)	T _{start} (UT)	Duration (min)	Class	Location	T _{peak} (UT)	β^{HPE}		Frequency (MHz)
1	1998-08-29	18:29	18:22	10	C5.3	200-50	1.1-1.4	2.1 ± 0.2 ^k
2	2001-10-09	07:38	249	126	529	6.9E+30*	200-50	1.1-1.4	...
3	2002-02-20	06:04	Halo	360	963	9.5E+30*	...	05:43	24	M5.1 N12W72	Yes ^h	...	95-57	1.3-1.4	1.1 ± 0.4
4	2002-10-20	11:28	248	15	918	11:12	25	C1.0	No ⁱ	22.0 ± 3.5 ^k
5 ^a	2002-10-20	14:08	247	20	1011	1.7E+30	...	14:02	11	C6.6 S13W63	No	...	180-25	1.1-1.7	171.9 ± 7.3 ^k
6	2003-03-17	10:06	No	12.0 ± 1.6
7	2005-09-04	15:01	286	86	1179	3.8E+31	...	13:59	133	C2.0 N13W72	Yes ^h
8	2011-08-08	17:54	269	33	757	3.8E+29	17:51	18	M3.5 N16W61	Yes ^h	135-25	1.2-1.7	0.8 ± 0.1
9	2013-11-12	21:35	259	35	302	1.5E+28	21:31	6	C3.1 S16W62	Yes	21:31	6.7 ± 0.2	6-0.4	2.6-13	3.5 ± 1.0 ^k
10	2014-02-20	07:45	Halo	360	969	3.9E+31*	07:37	59	M3.0 S15W73	Yes	07:36	4.5 ± 0.1	180-26	1.1-1.7	0.03 ± 0.53 ⁱ
							07:42				07:41	5.5 ± 0.1	12-7.7	2.0-2.3	

Notes.^(a) Also studied by Pick et al. (2006) and Wang et al. (2011, 2016).^(b) Solar release time of SEEs in the event's highest energy channel, the same as T_{rel} in Table A.1.^(c) Data from the SOHO/LASCO CME catalog (https://cdaw.gsfc.nasa.gov/CME_list/). K represents the CME kinetic energy, and a superscript star marks the values that are not reliable due to large uncertainties.^(d) No available data.^(e) Data from SDO/AIA at 171 Å. T represents the start time of jets at the Sun, estimated by subtracting 500 seconds from the onset time detected at 1 au. Event 9 and 10 are associated with two jets.^(f) Data from the GOES flare list (<ftp://ftp.swpc.noaa.gov/pub/warehouse/>), confirmed with GOES 1-8 Å observations. T_{start} is the start time of the flare at the Sun. Duration = end time - start time.^(g) Data from RHESXI. T_{peak} is the peak time of the flare at the Sun.^(h) HXR flares without (reliable) peak measurements.⁽ⁱ⁾ Influenced by South Atlantic Anomaly during the considered time interval.^(j) Data from the Solar Geophysical Data (ftp://ftp.ngdc.noaa.gov/STP/SOLAR_DATA/) and Wind/WAVES observations at <14 MHz. *r* is the derived heliocentric distance.^(k) Likely underestimated because the ⁴He is dominated by a previous large solar energetic particle event (Hart et al. 2024).^(l) An upper-limit estimate.

Table A.3. Comparison with general power-law SEE events

	SEE			Flare			West-Limb CME			Type II				
	$\beta(\beta_1)$	β_2	$E_{\text{bp}}(E_{\text{b}})$ (keV)	$J_{\text{pk}}^{2.8\text{keV}}/10^4$ (cm s sr keV) ⁻¹	$J_{\text{pk}}^{108\text{keV}}$ (cm s sr keV) ⁻¹	Ratio	Class	Duration (min)	HXR	Ratio	V (km/s)	Width (deg)	IP	Ground
Event 10	3.6 ± 0.5	1.7 ± 0.2	56 ± 6	2.5	64.6	Yes	M3.0	59	Yes	Yes	969	360	Yes	Yes
Other 9 events	$2.5^{+0.3}_{-0.3}$...	61^{+16}_{-5}	$0.25 - 12.6$	$0.6 - 128$	$79\% (7/9)$	$C5.3^{+20.8}_{-2.5}$	$18^{+24.5}_{-10.5}$	$57\% (4/7)$	$88\% (7/8)$	918^{+69}_{-275}	61^{+46}_{-34}	$11\% (1/9)$	$44\% (4/9)$
All 10 events	$2.6^{+0.7}_{-0.2}$...	59^{+18}_{-3}	$0.25 - 12.6$	$0.6 - 128$	$80\% (8/10)$	$C6.0^{+27}_{-3.4}$	$21^{+21}_{-10.5}$	$63\% (5/8)$	$89\% (8/9)$	941^{+49}_{-298}	61^{+46}_{-34}	$20\% (2/10)$	$50\% (5/10)$
SPL	$2.8^{+0.5}_{-0.2}$	$0.12 - 6.2$	$0.017 - 7.2$	70%	$C1.0^{+8.7}_{-0.9}$	19^{+19}_{-10}	38%	76%	720^{+290}_{-170}	56^{+102}_{-11}	13%	N/A ^b
UDPL	$3.0^{+0.3}_{-0.3}$	$2.2^{+0.2}_{-0.3}$	$5.1^{+4.2}_{-1.8}$	$0.096 - 8.9$	$0.012 - 65$	74%	$M1.7^{+3.4}_{-1.6}$	30^{+11}_{-16}	64%	90%	1000^{+550}_{-120}	71^{+83}_{-53}	47%	N/A ^b
DDPL $_{E_{\text{b}} < 20\text{keV}}$	$2.0^{+0.2}_{-0.2}$	$3.3^{+0.5}_{-0.3}$	$5.6^{+2.3}_{-2.4}$	$0.12 - 22$	$0.019 - 230$	79%	$C1.2^{+3.0}_{-1.3}$	24^{+6}_{-13}	55%	85%	540^{+290}_{-150}	52^{+67}_{-38}	8%	N/A ^b
DDPL $_{E_{\text{b}} \geq 20\text{keV}}$	$2.1^{+0.3}_{-0.3}$	$3.9^{+0.6}_{-0.7}$	61^{+23}_{-12}	$0.029 - 38$	$0.011 - 150$	80%	$C2.0^{+1.1}_{-1.7}$	$14^{+17}_{-6.7}$	76%	91%	610^{+350}_{-240}	70^{+49}_{-30}	20%	N/A ^b

Wang et al. (2024)

Notes.^(a) The spectral parameters (β , E_{bp}) are obtained from MUL fitting results.^(b) Not provided by Wang et al. (2024).